

GEMS: WHICH GALAXIES DOMINATE THE $z \sim 0.7$ ULTRAVIOLET LUMINOSITY DENSITY?

C. WOLF,¹ E. F. BELL,² D. H. MCINTOSH,³ H.-W. RIX,² M. BARDEN,² S. V. W. BECKWITH,^{4,5} A. BORCH,²
J. A. R. CALDWELL,⁴ B. HÄUSSLER,² C. HEYMANS,² K. JAHNKE,⁶ S. JOGEE,⁴ K. MEISENHEIMER,²
C. Y. PENG,⁷ S. F. SÁNCHEZ,⁶ R. S. SOMERVILLE,⁴ AND L. WISOTZKI⁶

Received 2004 August 16; accepted 2005 April 28

ABSTRACT

We combine high-resolution images from GEMS with redshifts and spectral energy distributions from COMBO-17 to explore the morphological types of galaxies that dominate the $z \sim 0.7$ UV luminosity density. We analyzed rest-frame 280 nm and V -band luminosities of 1483 galaxies with $0.65 < z < 0.75$, combining these with visual morphological classifications from F850LP images (approximately rest-frame V band) taken with *HST* ACS on the Extended Chandra Deep Field–South. We derive UV luminosity functions and j_{280} luminosity densities for spheroid-dominated galaxies, spiral galaxies, Magellanic irregular galaxies, and clearly interacting galaxies with morphologies suggestive of ongoing major mergers. We check the reliability of GEMS morphologies against the deeper GOODS images and quantify an incompleteness of the GEMS merger identification at the faint end. We derive the fractions of the global UV luminosity density j_{280} originating from the galaxy types and find that spiral and Magellanic irregular galaxies dominate with about 40% each. Interacting and merging galaxies account for roughly 20% of j_{280} , while the contribution of early types is negligible. These results imply that the strong decline in the UV luminosity density of the universe observed from $z \sim 1$ until today is dominated by the decreasing UV luminosities of normal spiral galaxies, accompanied by the migration of UV-luminous star formation in irregular galaxies to systems of progressively lower mass and luminosity. These conclusions suggest that major-merger–driven star formation cannot dominate the declining cosmic star formation rate, unless major mergers are substantially more obscured than intensely star-forming spiral galaxies *and* the decline in observed cosmic star formation rate is substantially stronger than the already precipitous decline in uncorrected UV luminosity density.

Subject headings: galaxies: evolution — galaxies: general — galaxies: luminosity function, mass function — surveys

1. INTRODUCTION

It is well established that the UV luminosity density integrated over the galaxy population drops from $z \gtrsim 1$ to the present day (Madau et al. 1996, 1998; Lilly et al. 1996; Cowie et al. 1996), amounting to a factor of 3 to 6 decline between $z = 0.7$ and $z = 0$ at $\lambda_{\text{rest}} = 280$ nm (Lilly et al. 1996; Cowie et al. 1996; Wilson et al. 2002; Wolf et al. 2003).⁸ Because UV light is emitted by young, massive stars, this decline is conceptually linked to a dramatic decline in the global cosmic star formation rate (SFR). Despite the fact that most UV photons are absorbed by dust (Wang & Heckman 1996), observations of less dust sensitive SFR indicators support this interpretation (Flores et al. 1999; Haarsma et al. 2000; Yan et al. 1999), although they do not reach as far down the luminosity function. The goal of this paper is to explore the physical processes driving the evolution of the cosmic SFR by investigating the contribution of different

galaxy morphological types to the cosmic-averaged UV luminosity density at $z \sim 0.7$, when the universe was half of its present age.

The physics that drives this decline remains unclear. Observations of damped Ly α systems and local H I surveys indicate that the cosmic density of cold neutral gas also declines dramatically from $z \sim 1$ to the present (e.g., Storrie-Lombardi et al. 1996). Some of the decline in cold gas is simply because a significant fraction of the available baryons become locked up in long-lived stars (Pei et al. 1999). The hierarchical formation of massive structures at $z \lesssim 2$ also leads to a larger fraction of gas being in a shocked warm/hot phase, with long cooling times (e.g., Cen & Ostriker 1999), contributing further to the declining cosmic cold neutral gas density. If the efficiency of star formation is linked to the surface density of gaseous disks, as suggested by local observations (Kennicutt 1998), and if gas disks are denser at high redshift, this alone may dominate the declining cosmic SFR (Somerville et al. 2001). Yet, galaxy interactions are known to trigger efficient bursts of star formation (e.g., Sanders & Mirabel 1996); it is likely that a decline in the merger rate (Le Fèvre et al. 2000; Carlberg et al. 2000; Patton et al. 2002; Conselice et al. 2003; Bundy et al. 2004; although see Lin et al. 2004 for a different conclusion) will also contribute to the declining SFR over this period.

The characteristic rise and decline of the cosmic SFR is a generic prediction of cosmological simulations of galaxy formation in the cold dark matter framework (Baugh et al. 1998; Somerville et al. 2001; Nagamine et al. 2000; Springel & Hernquist 2003; Hernquist & Springel 2003). But the location of the SFR maximum and the rate of the decline depend on the input physics,

¹ Department of Physics, Denys Wilkinson Building, University of Oxford, Keble Road, Oxford OX1 3RH, UK.

² Max-Planck-Institut für Astronomie, Königstuhl 17, D-69117 Heidelberg, Germany.

³ Department of Astronomy, University of Massachusetts, 710 North Pleasant Street, Amherst, MA 01003.

⁴ Space Telescope Science Institute, 3700 San Martin Drive, Baltimore, MD 21218.

⁵ Johns Hopkins University, Charles and 4th Street, Baltimore, MD 21218.

⁶ Astrophysikalisches Institut Potsdam, An der Sternwarte 16, D-14482 Potsdam, Germany.

⁷ Steward Observatory, University of Arizona, 933 North Cherry Avenue, Tucson, AZ 85721.

⁸ In this paper we assume $(\Omega_m, \Omega_\Lambda) = (0.3, 0.7)$ and $H_0 = h \times 100 \text{ km s}^{-1}$.

especially the treatment of star formation and feedback. Hence, observational tests of star formation in different types of galaxies are very interesting for constraining these model ingredients.

In this paper we present progress toward pinning down the underlying physics responsible for the decline in the cosmic SFR, through an investigation of the contribution of galaxies with different morphological types to the UV luminosity density at $z \sim 0.7$. For this investigation we combine high spatial resolution imaging from the Advanced Camera for Surveys (ACS) on the *Hubble Space Telescope* (*HST*)—taken from the GEMS (Galaxy Evolution from Morphology and SEDs; Rix et al. 2004) survey—with accurate photometric redshifts and rest-frame UV/optical luminosities and colors from COMBO-17 (Classifying Objects by Medium-Band Observations in 17 Filters; Wolf et al. 2001, 2004). In particular, we will assess the UV luminosity contribution of manifestly interacting or morphologically peculiar galaxies at $z \sim 0.7$ compared to, e.g., luminous spirals. We restrict our attention to a redshift slice at $0.65 < z < 0.75$, where the ACS F850LP band corresponds roughly to the rest-frame V band, in order to bypass uncertainties due to morphological K -corrections and to minimize any redshift-dependent selection effects, e.g., due to cosmological surface brightness dimming. Our sample contains almost 1500 galaxies with COMBO-17 redshifts and visually classified morphological types. A more detailed study over the full redshift range probed by the GEMS sample will be presented in future work.

The rest-frame UV luminosity is an important tracer for star formation all the way to $z \gtrsim 6$ (e.g., Sullivan et al. 2000; Giavalisco 2002; Bouwens et al. 2003; Bunker et al. 2004). Of course, a fuller understanding of how the SFR density evolves will have to incorporate complementary constraints on the bolometric luminosity of the youngest stellar population, such as $H\alpha$, IR, or radio luminosities. In order to directly constrain the amount of dust-obscured star formation in our sample, a first analysis of *Spitzer Space Telescope* 24 μm data taken by the MIPS instrument team (Rieke et al. 2004) on the Chandra Deep Field–South is presented in a companion paper (Bell et al. 2005). However, the advantage of the UV analysis presented here is that observations of rest-frame UV probe much further down the luminosity function than all other SFR indicators at $z \gtrsim 0.5$, meaning that the total UV luminosity density is relatively reliably constrained. Finally, this study will reveal which galaxies are responsible for the changing UV ionizing background at $z \lesssim 1$, because galaxies with large contributions to the 280 nm luminosity density are likely to make correspondingly large contributions to the cosmic luminosity density in the ionizing background at $\lambda < 91$ nm.

The structure of this paper is as follows. In § 2 we describe the data sets, and in § 3 our morphological classification. In § 4 we discuss the distribution of UV/optical galaxy colors, present UV luminosity functions by morphological type, and assess the contribution of different types to the rest-frame UV luminosity density. In § 5 we discuss our results in the light of previous results and theoretical predictions, summarizing in § 6.

2. DATA

The COMBO-17 survey has measured accurate photometric redshifts for more than 10,000 galaxies in the Extended Chandra Deep Field–South (ECDF-S; Wolf et al. 2004). The redshifts are estimated using data from five broad and 12 medium bands. We use seeing-adaptive aperture photometry measuring the same physical fraction of a galaxy in each passband and concentrate the aperture on the brighter central parts. This way we ensure a maximum signal-to-noise ratio for recovering the spectral energy distribution (SED) and redshift of any object (see Wolf et al.

2004 for all details). Detailed comparisons with spectroscopic redshifts and simulations have suggested the mean error of COMBO-17 redshifts to be $\sigma_z/(1+z) \sim 0.02$ for galaxies with $R < 23$ and $z < 1.2$. COMBO-17 has also identified type 1 active galactic nuclei (AGNs) when the contribution of AGN light to the SED was sufficient to leave recognizable traces in the 17 band data set.

The GEMS survey has covered almost the whole COMBO-17 area on the ECDF-S with *HST* ACS observations on an area of ~ 800 arcmin² (J. A. R. Caldwell et al., in preparation; Rix et al. 2004). Altogether, 77 *HST* ACS pointings were observed with an exposure time of one orbit each in the F606W and F850LP passbands. The central one-fifth of the area is incorporated from the first epoch of GOODS (Great Observatories Origins Deep Survey) imaging (Giavalisco et al. 2004).⁹ For galaxy classification, the images are approximately surface brightness–limited, at a limiting average surface brightness within the half-light radius of $z_{\text{AB}} \sim 24$ mag arcsec⁻² in the F850LP passband.

For this paper we have selected all galaxies from the overlapping area of COMBO-17 and GEMS, which have no measurable type 1 AGN contribution, photometric redshifts of $0.65 < z < 0.75$, and aperture magnitudes of $R_{\text{aper}} < 24$. At $R_{\text{aper}} < 24$ our photometric redshifts are well behaved and their completeness is well understood. We have removed three objects (of 1486) because their unusually high luminosities in excess of $M_{280} = -22$ place them far off the main sample. These galaxies are likely to have strong contributions from an unrecognized AGN, supported by an *XMM-Newton* detection of the one $M_{280} < -22$ galaxy that lies in the *XMM* area.

The galaxy sample used here covers the redshift spikes of the galaxy distribution in the CDF-S at $z = 0.67$ and $z = 0.73$ (Gilli et al. 2003; Le Fèvre et al. 2004). At this redshift the observed ACS F850LP band corresponds to the rest-frame V band. Altogether, the sample contains 1483 galaxies and fills a comoving volume of 42,375 (Mpc h^{-1})³. Although the slice selects the highest density environments known in the CDF-S, it contains no massive clusters. At most redshifts, the CDF-S is observed to be rather underdense compared to the cosmic average. However, this is currently still the largest sample of moderately distant galaxies with redshifts and wide-field space-based data from which morphology can be determined.

The photometric redshift quality of our specific sample is demonstrated in Figure 1. We have spectroscopic redshifts from the VIMOS VLT Deep Survey (VVDS; Le Fèvre et al. 2004) for $\sim 10\%$ of the galaxies in our sample (with VVDS redshift reliability of 95% or greater). We find three outliers among 152 galaxies (2%) with true redshift errors on the order of 0.1, while the remaining 98% of the sample have a distribution of photo- z errors $\delta_z = z_{\text{spec}} - z_{\text{phot}}$ of

$$\delta_z/(1+z) = -0.006 \pm 0.020. \quad (1)$$

The COMBO-17 filters have central wavelengths ranging from observed-frame 365 to 915 nm and allow us to calculate galaxy luminosities anywhere from 220 to 550 nm rest-frame wavelength directly from observed photometry with no need for extrapolations or externally estimated K -corrections. We obtain rest-frame luminosities by placing the best-fitting template SED into the observed 17 filter spectrum and integrating

⁹ Below we compare morphological classifications from first-epoch GOODS imaging with the full-depth GOODS imaging to explore how the results from GEMS may be systematically biased by the shallower imaging data.

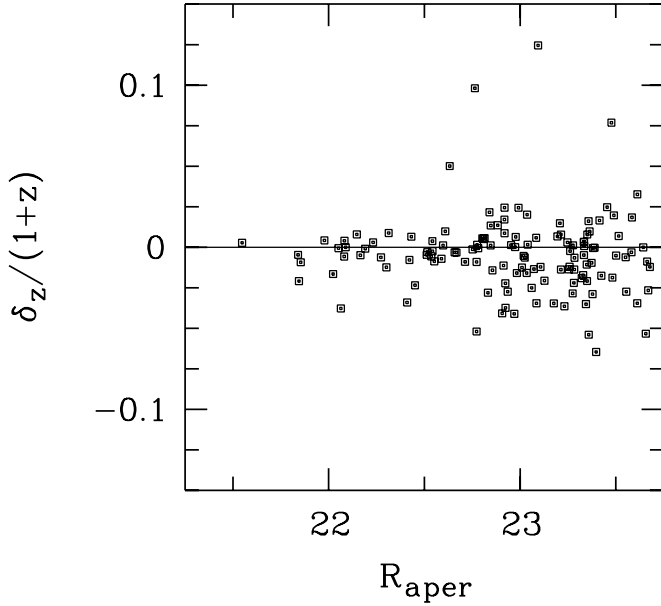


FIG. 1.—Redshift errors. The VVDS survey provides redshifts with $>95\%$ reliability for 152 of the 1483 galaxies in our sample. Three outliers can be seen with redshift errors on the order of $\delta_z \sim 0.1$. The bulk of the sample (98%) have a mean offset from the spectroscopic redshift of $\langle \delta_z / (1+z) \rangle = -0.006$ and an rms scatter of 0.020 in terms of $\delta_z / (1+z)$.

the template over the efficiency curve of the desired redshifted rest-frame band. Here the template is normalized to match the total R -band photometry rather than the aperture photometry to include all measurable flux from the object and get a total luminosity. Since the shape of the SED is still determined from aperture photometry, we measure only central colors for large, nearby galaxies and are thus insensitive to color gradients in those. We choose to explore the rest-frame band Johnson UBV and a synthetic 280/40 band centered on 280 nm with a rectangular transmission function and width of 40 nm. We estimate errors for rest-frame luminosities and colors in COMBO-17 on the basis of the errors of the photometry itself (for details, see Wolf et al. 2004). These should not exceed 0.2 mag including systematic aperture and calibration biases in most cases.

In Figure 2 we present a completeness map for our sample, which is used later for the calculation of luminosity functions. This map has been constructed from end-to-end Monte Carlo simulations of the COMBO-17 survey that use a variety of object SEDs as an input; their photometric properties and subsequent classification are based on aperture colors, using the standard COMBO-17 procedure. The input SEDs span the entire range of assumed possible spectra from the libraries of stars, galaxies, and QSOs that are used in COMBO-17 for classification and redshift estimation. The map shows completeness in dependence of apparent total R -band magnitude and the rest-frame color $U - V$. At $R_{\text{tot}} > 24$ our completeness is zero because of the aperture magnitude cut ($R < 24$) and because any total magnitude is brighter than or equal to the aperture magnitude. The gentle rise of the completeness to brighter magnitudes stems from the distribution of aperture corrections, $R_{\text{tot}} - R_{\text{aper}}$, and from increasing completeness in photo- z determination. The photo- z completeness refers to the fact that in COMBO-17 objects are not assigned any redshift if the probability distribution $p(z)$ is too wide and hence the expected redshift error too large, which happens more often among faint objects (see Wolf et al. 2004 for more details). Accordingly, the 50% completeness limit corresponds to $R_{\text{tot}} \approx 23.7$, and the 90% completeness limit to $R_{\text{tot}} \approx 23$.

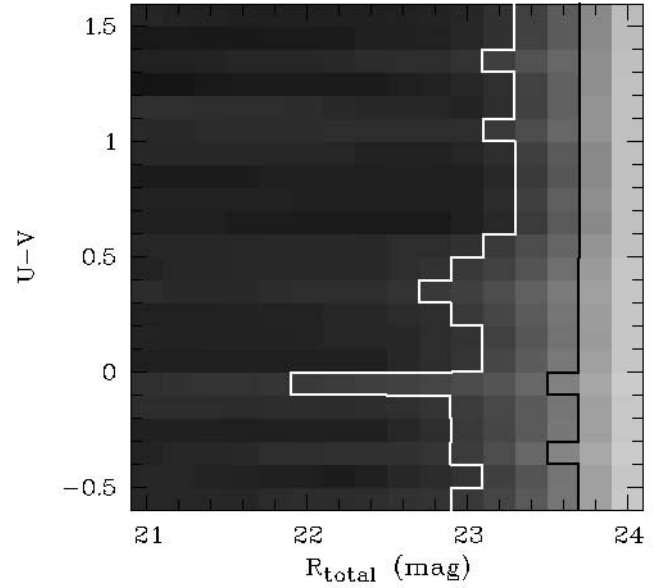


FIG. 2.—Sample completeness. Monte Carlo simulations of the COMBO-17 survey with classification and redshift estimation yield this map of completeness for galaxies at $0.65 < z < 0.75$. Dark gray denotes high completeness, and light gray denotes low completeness. Lines are drawn at 50% completeness (black) and 90% (white). At $R < 23$ the sample is more than 90% complete, and at $R = 23.7 \sim 50\%$ of the galaxies are still included. At $R > 24$ no galaxy is included, because of the $R_{\text{aper}} < 24$ selection cut.

In terms of rest-frame selection, our observed frame cut in the R band corresponds at $z \sim 0.7$ to a band in rest frame centered on 380 nm and with 115 nm width. Apart from the width, this is similar to a rest-frame U -band selection. As a last sanity check for our sample, we explore the derived rest-frame colors $M_{280} - M_U$ and $U - V = M_U - M_V$, since we make frequent use of the M_{280} and M_V measurements in this paper. From Figure 3 we conclude that the entire galaxy sample follows almost a

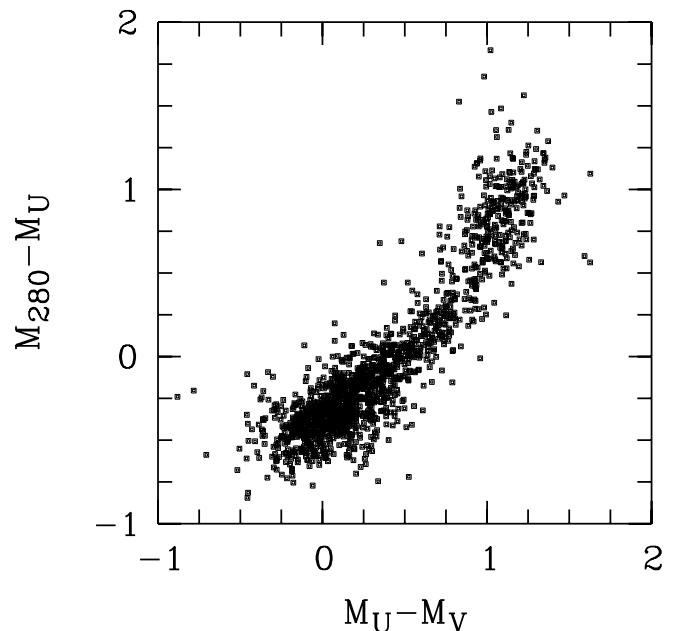


FIG. 3.—Rest-frame colors. The sample galaxies form almost a one-parameter family in near-UV–optical rest-frame colors. The bimodality can be seen as well.

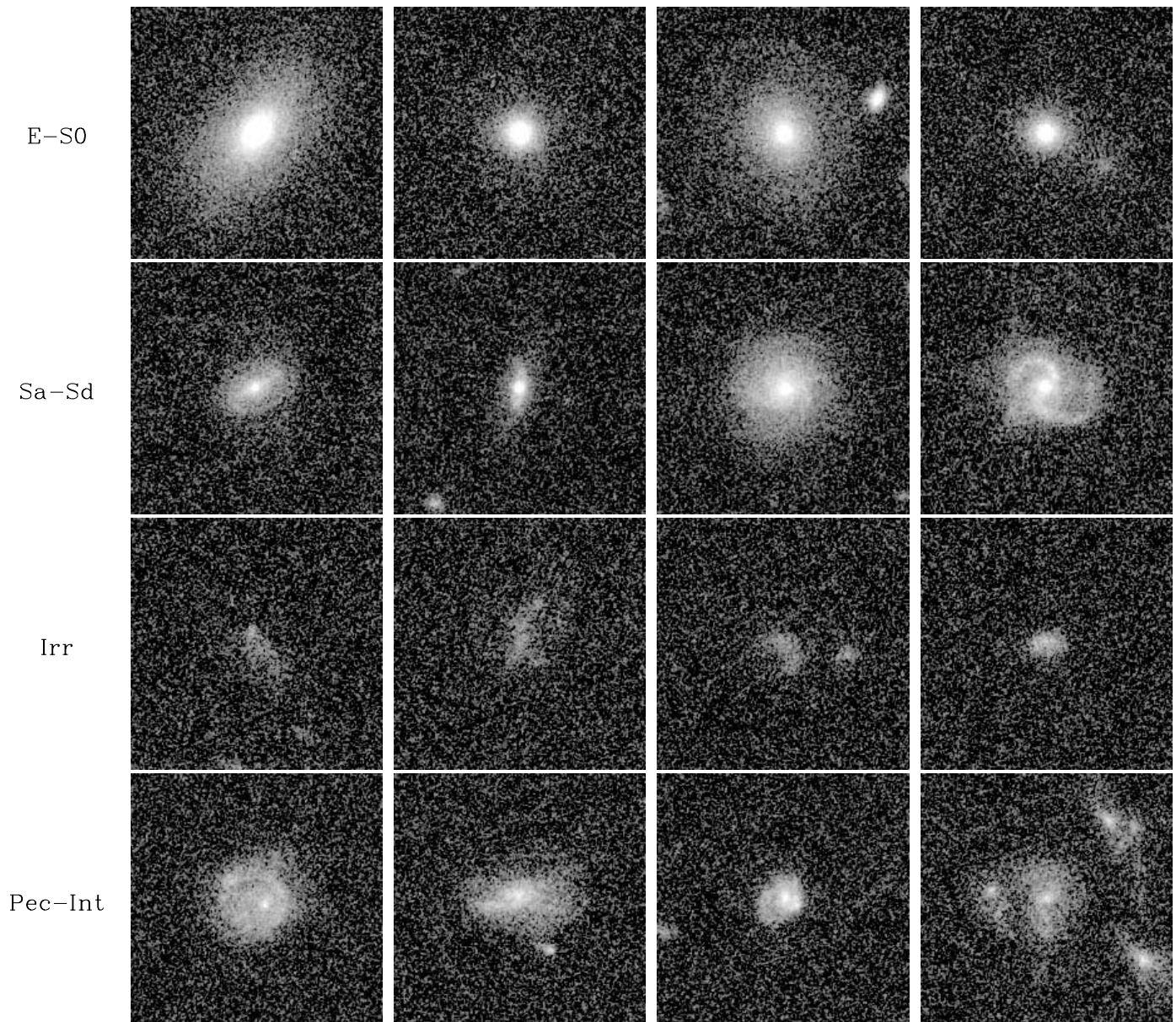


FIG. 4.—*HST* ACS F850LP example images of the four broad bin types; each class has four examples. Panels measure $6'' \times 6''$, corresponding to roughly $45 \text{ kpc} \times 45 \text{ kpc}$. From top row to bottom row: E–S0, Sa–Sd, Irr, and Pec–Int.

one-parameter family for rest-frame colors between 280 nm and V band. Galaxies are either generally blue or generally red. In particular, there are no galaxies that combine blue $M_{280} - M_U$ colors with red $U - V$ colors, i.e., galaxies where the rest-frame U band and thus the observed-frame R band would be unexpectedly faint. We conclude that average one-parameter color-color transformations are sufficient to describe the sample. Hence, it is trivial to transform our observed-frame R -band completeness map into a rest-frame M_{280} -band or V -band map.

3. MORPHOLOGICAL CLASSIFICATIONS

Morphological classification was carried out by eye on the F850LP images for the complete sample of 1483 $0.65 < z < 0.75$ galaxies. Galaxies were classified into a final set of four broad classes. These four are the following: spheroids (E–S0), spirals (Sa–Sdm), irregulars (Irr), and morphologically peculiar galaxies with disturbances suggestive of interaction and ongoing major mergers (Pec–Int).

In Figure 4 we show examples of these four classes. Galaxies with dominant centrally concentrated light profiles and lacking spiral structure were classified as elliptical (in the case where no evidence for a disk was seen) or S0 (in the case where a smooth disk was seen); these two classes are illustrated in the top panels of Figure 4. Galaxies with prominent disks and spiral structure were classified as Sa–Sd; where Sa galaxies have strong bulges and tightly wound spiral structure through to Sd galaxies with no bulge and prominent, flocculent, and often disorganized spiral structure (the second row of examples). Galaxies with an irregular appearance suggestive of stochastic star formation, similar to Magellanic irregular galaxies in the local universe, were classified as irregular (the third row of examples).¹⁰ A significant number of galaxies appeared to be undergoing mergers

¹⁰ The small number of galaxies that were too compact to reliably classify were included in the irregular bin: these galaxies were faint and very blue and are likely high-redshift analogs to the blue compact dwarf galaxies seen in the local universe.

or tidal interactions: these were classified in the Pec-Int category (the final row of examples in Fig. 4). Galaxies were classified as merging or interacting if they have multiple nuclei, strongly distorted inner isophotes, or large tidal features. These visual signatures are primarily tracers of major mergers (mass ratios of 1:1 to 1:4 according to Somerville et al. 2001), but they also trace some minor mergers with mass ratios up to 1:10 (as assessed by doing aperture photometry of some interacting pairs).

The visual classification of merging and interacting galaxies is clearly subjective, but automated classification also presents a serious challenge owing to the richness of structure in both normal spirals and interacting systems. Issues such as source extraction and segmentation, projection of very close galaxy pairs, and recognition of faint, low surface brightness tidal tails in otherwise largely relaxed systems are all important and not easily modeled automatically (see Conselice 2003; Lotz et al. 2004 for current progress on some of these issues). For this reason, we chose to explore visually classified morphology at this time, deferring an analysis based on automated classification to a later stage.

We estimate the variance of this classification process by having three of the authors (E. B., D. M., and C. W.) classify the entire sample independently. Our fine classification scale ran along the types (E, S0, Sa, Sbc, Sd, Irr, Pec-Int). Between authors classifications differed by ± 1 class or fewer for 80% of the sample. The classifications of galaxies in the faintest magnitude bin differed the most frequently, owing to the small size and low surface brightness of these galaxies. These difficulties in classifying faint galaxies led to two effects: first, random scatter in the classification increases as the by-eye classification becomes more ill-defined; second, at low signal and for small galaxies interaction features cannot be discerned, which will bias the classification systematically against peculiar galaxies (Pec-Int).

We reduce the effect of random scatter onto our results by using the classifications of all three authors with a weight of one-third each. When we calculate luminosity functions, e.g., we include the author-to-author variation besides Poisson noise in the error analysis. This variation dominates errors at faint levels, while Poisson noise reigns at the bright end, where object numbers are small and classifications agree most frequently.

In order to assess systematic biases among faint galaxies, we also analyze the deeper five-epoch GOODS images, which cover one-fifth of the entire GEMS area. This subsample was classified again by the same authors and compared against the results from the shallower one-epoch GOODS images that are incorporated into GEMS. From this comparison, we have found that all classifiers find a significantly larger fraction of faint Pec-Int galaxies in the five-epoch GOODS data than in the GEMS data. The GEMS classifications of these extra Pec-Int galaxies included some early types and spirals, but were dominated by irregulars; the extra depth afforded by GOODS allowed for the recognition of faint tidal features not visible in the shallower GEMS data. This source of uncertainty is discussed further below when we determine the relative contributions of different morphological types to the UV luminosity density. In contrast, we see no significant differences among other morphological types, suggesting that these are easily recognized and unbiased.

4. RESULTS

4.1. Colors and Magnitudes

In Figure 5 we plot the near-UV–optical color-magnitude diagrams (CMDs) for our sample split by morphological type. The CMDs of our sample are bimodal, having a “red sequence”

of mostly non–star-forming galaxies and a “blue cloud” of star-forming galaxies. This bimodality of galaxy colors at optical wavelengths has been observed in the local universe (Strateva et al. 2001; Baldry et al. 2004) and out to $z \sim 1$ (Bell et al. 2004). Owing to the long-wavelength base between 280 nm and the V band ($\lambda_V/\lambda_{280} \sim 2$) and the sensitivity of the UV spectrum to ongoing star formation, galaxies span 4 mag in rest-frame ($M_{280} - M_V$) color.

The observed-frame $R < 24$ selection translates into a UV luminosity detection limit that changes with ($M_{280} - M_V$) color. As we can see in the left-hand panel of Figure 5, increasingly red galaxies of given visual magnitude appear at decreasing M_{280} luminosities; hence the sample looks increasingly deep toward the red. The sample selection has no sharp cutoff at its faint end, because the COMBO-17 redshift completeness declines before reaching $R = 24$. In Figure 5 we also plot a rough cut for a brighter subsample that is at least 90% complete. This particular subsample is used for the color distributions plotted in Figure 6.

The four right-hand panels in Figure 5 demonstrate how galaxies of each morphological type populate the CMD. E–S0 galaxies populate primarily the red sequence; however, there are also some blue galaxies with smooth appearance and high light concentration. Examples of such potential blue spheroids have been seen before at a range of redshifts (e.g., Menanteau et al. 2001). Their fraction among the total spheroid population is around 30%–40%, depending on rest-frame band (UBV), magnitude limits and choice of the red-sequence cut for their selection. It is interesting to note that in CMDs with optical or near-infrared luminosities, the most luminous galaxies are typically red spheroid-dominated galaxies. In the UV, these red galaxies are in fact somewhat fainter, on the whole, than the brightest star-forming spirals and interactions, owing to their color. Selecting a spheroid sample in the rest-frame UV naturally increases the fraction of blue members to, e.g., 62% at $M_{280} < -19$.

Spiral galaxies (Sa–Sd) are mostly found in the blue cloud but have a tail extending up to the red sequence. Presumably, this tail in the color distribution is partly due to dust reddening, in particular for edge-on spirals, but in some cases it reflects very low levels of ongoing star formation. Irregular galaxies have rather lower luminosities and are almost exclusively blue, presumably because of star formation and little overall obscuration.

Visually identified mergers (Pec-Int) are concentrated toward the blue end of the color distribution, but some lie on or near the red sequence. Most interacting galaxies on the red sequence show clear dust lanes, but some are high-inclination objects or almost regular spheroids with leftover tidal features. The mergers tend to have luminosities above average; this is partially a result of our known bias against faint interactions in the GEMS data (see § 3). However, a large fraction of the very bluest and most luminous galaxies are interactions, reflecting the important role of interaction-induced star formation in at least some fraction of galaxies.

Overplotting a line of estimated constant stellar mass of $10^{10} h^{-2} M_\odot$ in Figure 5 (simply based on observed colors and luminosities, following Bell & de Jong 2001), we see irregulars predominantly below this cut. Spheroids are weighted toward higher stellar masses. Major-merger candidates spread in a range of masses around the cut. Disk galaxies do the same, but with a tail to low masses.

Figure 6 shows the number counts of the morphological samples against rest-frame color. Here we use only the >90% complete subsample to avoid any bias due to color-dependent incompleteness or increased classification uncertainties at faint

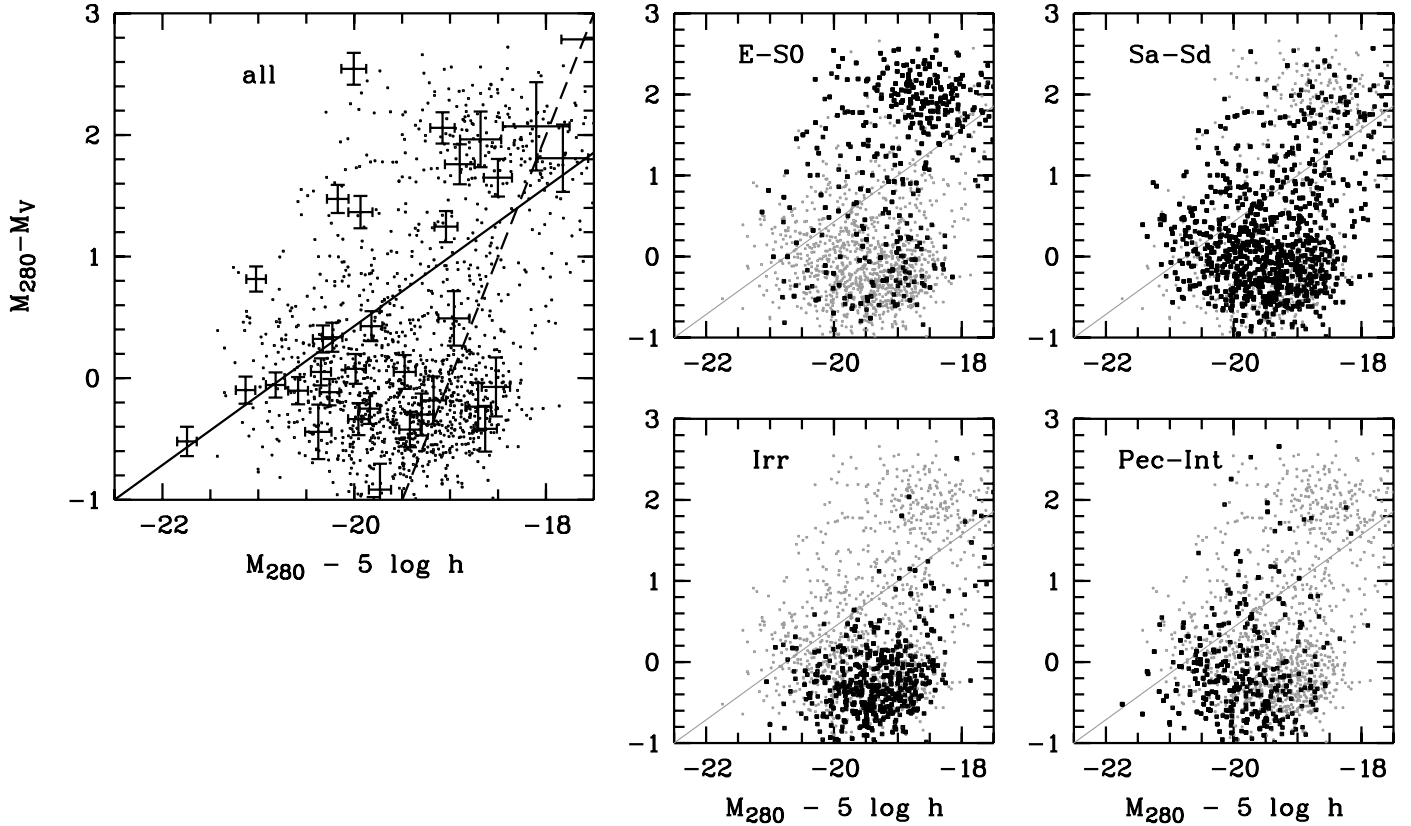


FIG. 5.—CMD. *Left*: The parent sample with 1483 galaxies. Error bars are given for a randomly chosen subsample; the error bars include expected systematic biases. The solid line roughly represents galaxies with constant mass of $10^{10} h^{-2} M_{\odot}$, following Bell & de Jong (2001). The dashed line delineates a subsample with $>90\%$ completeness. *Right*: Four panels showing the distribution of colors and magnitudes of the four different morphological types from all three classifiers combined (black dots) on top of the parent sample (gray background dots).

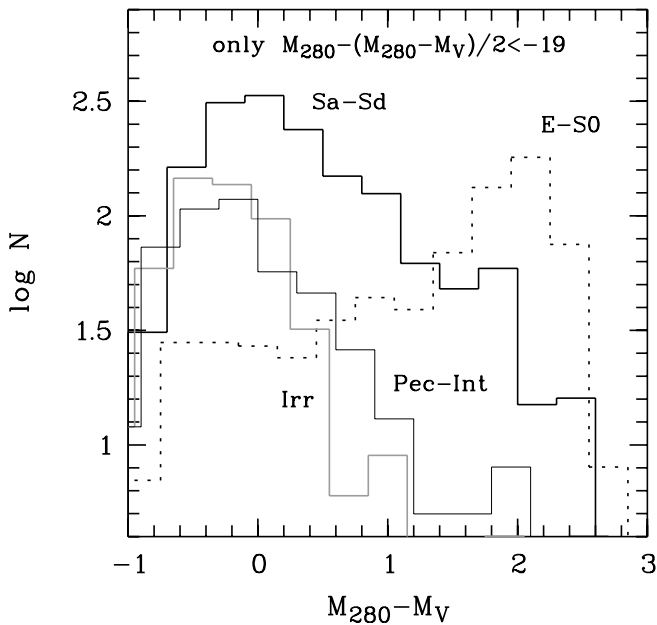


FIG. 6.—Rest-frame color distribution for different morphological types. Spheroids (E-S0) are predominantly red, irregulars almost uniquely very blue. Spirals and major mergers (Pec-Int) have somewhat similar distributions, with mostly blue objects and a tail to the red. Here we only used galaxies from a brighter subsample that is at least 90% complete.

limits. This selection is defined by $M_{280} - (M_{280} - M_V)/2 < -19$ and is illustrated in the left-hand panel of Figure 5 as the dashed line. We find the color distribution of Pec-Int galaxies to be somewhat similar to that of normal spirals (and quite different from that of irregulars). Aside from the different amplitude of the two distributions, the color of the Pec-Int peak is only slightly bluer than that of spirals, and the tail to the red mimics that of the spirals. The similarity may reflect the compensating effects of enhanced star formation and enhanced dust obscuration in mergers, while the merging partners originate mostly from the spiral sample.

4.2. Luminosity Functions

Near-UV luminosity functions (LFs) for the four different galaxy types in the rest-frame 280 nm passband are presented in Figures 7 and 8. We adopt a $M_{280} \lesssim -19$ limit for LF calculation to ensure that galaxies of all rest-frame colors are represented at least with 50% completeness. This way we ensure that the correction applied to $\phi(M)$ from our completeness maps never exceeds a factor of 2. This cut corresponds to $R \lesssim 23.5$ for the bluest star-forming galaxies and to $R \lesssim 22$ for red-sequence galaxies (see Wolf et al. 2003 for all equations and technical details on completeness and luminosity functions).

We present three sets of rest-frame UV LFs in this paper. In Figure 7 we show the LFs of the entire GEMS sample, split by morphological type. However, comparison between classifications derived from the 5 times deeper GOODS data and GEMS classifications demonstrated that the GEMS data are less sensitive to lower luminosity interactions than the GOODS data.

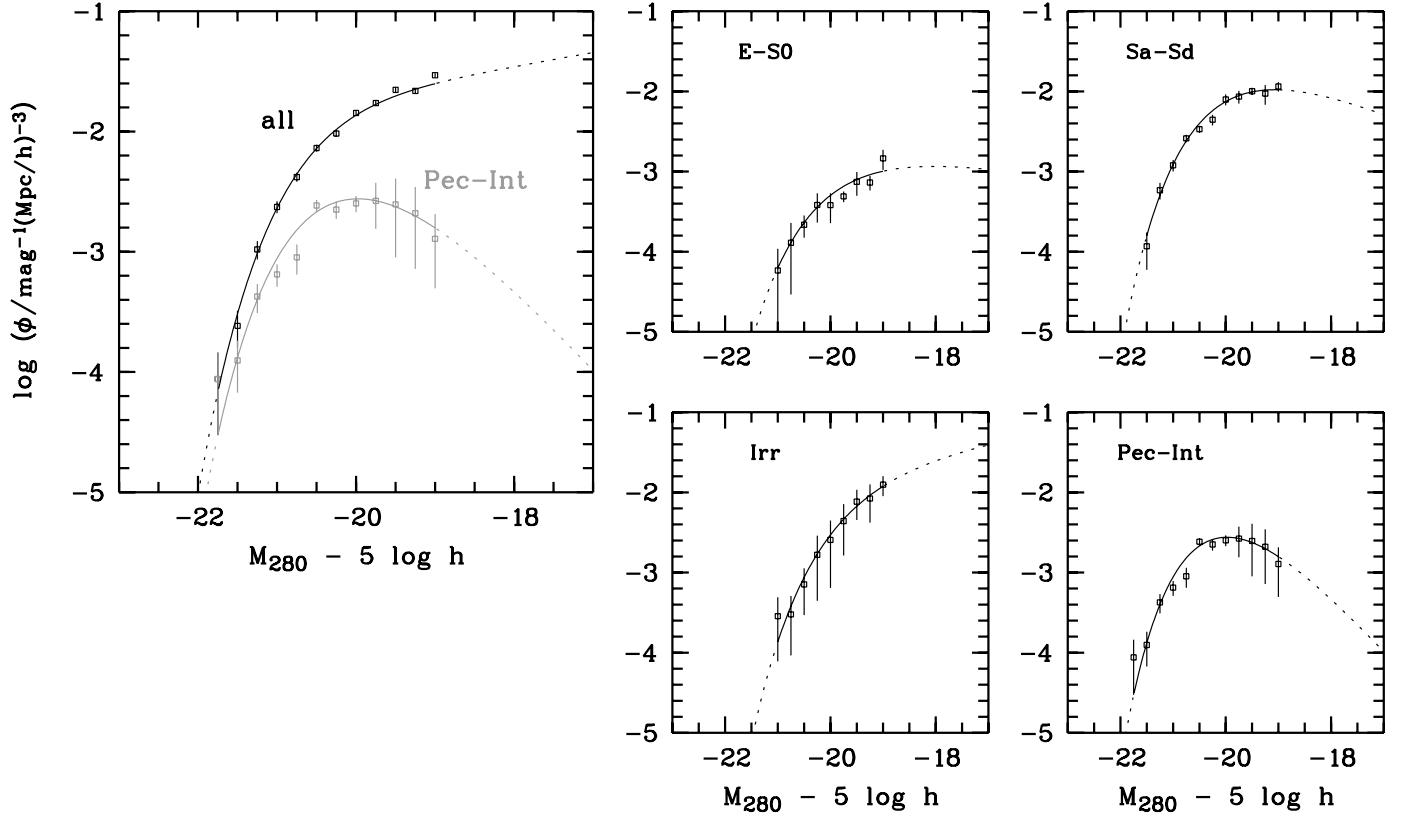


FIG. 7.—Near-UV luminosity functions from GEMS. *Left*: Parent sample with all galaxies, compared to clearly interacting galaxies. Lines are best-fitting Schechter functions. *Right*: The four morphological types, E-S0 (spheroids), Sa-Sd (spirals), Irr (irregulars), and Pec-Int (clearly interacting galaxies). Error bars are from Poisson noise or author-to-author variation from their independent morphological classifications, whichever is greater.

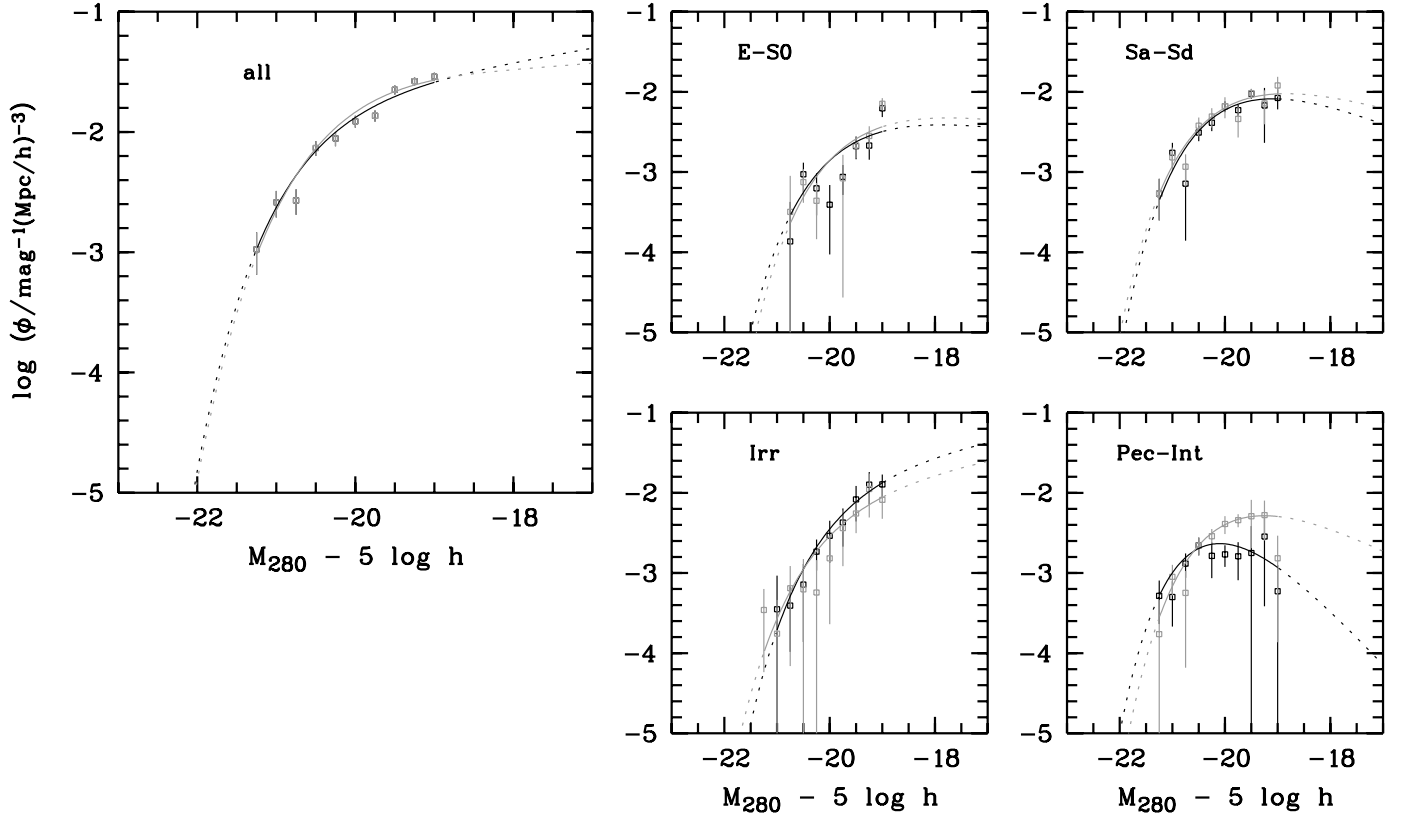


FIG. 8.—Near-UV luminosity functions from GOODS-shallow vs. GOODS-deep. The image depth influences our morphological classifications, an effect that propagates into the luminosity functions by type. Here we compare the LFs derived from the 290 galaxies from the GOODS area using both GEMS-depth and GOODS-depth data to separate classification differences from cosmic variance. The GEMS result is shown in black, and the GOODS result in gray. The major difference is that the LF of Pec-Int galaxies is increased at the faint end, while irregulars are lower by a similar amount.

TABLE 1
RESULTS OF STY FITS OF THE 280 nm LUMINOSITY FUNCTIONS

Sample	$M^* - 5 \log h$ (Vega mag)	$\phi^* \times 10^{-4}$ ($h \text{ Mpc}^{-1}$) ⁻³	α	$j \times 10^7 L_\odot$ ($h \text{ Mpc}^{-3}$)	c_{ϕ^*, L^*}
GEMS					
E-S0	-19.53 ± 0.19	22.83 ± 6.56	-0.75 ± 0.13	$6.22 \pm 1.79^{+0.29}_{-0.22}$	-0.906
Sa-Sd	-19.49 ± 0.11	285.93 ± 45.45	-0.32 ± 0.17	$74.28 \pm 11.81^{+2.43}_{-1.74}$	-0.779
Irr	-19.33 ± 0.17	239.70 ± 132.52	-1.31 ± 0.20	$78.53 \pm 43.41^{+23.95}_{-14.19}$	-1.686
Pec-Int	-19.33 ± 0.16	62.04 ± 19.17	0.82 ± 0.43	$26.20 \pm 8.10^{+1.40}_{-0.81}$	-0.162
All	-19.67 ± 0.16	556.35 ± 51.87	-0.75 ± 0.20	$185.23 \pm 45.73^{+24.13}_{-14.33}$	-0.943
GOODS					
E-S0	-19.25 ± 0.37	93.35 ± 11.74	-0.75 ± 0.13	$19.56 \pm 2.46^{+1.12}_{-0.90}$	-1.140
Sa-Sd	-19.64 ± 0.31	222.27 ± 61.72	-0.52 ± 0.41	$64.89 \pm 18.02^{+8.64}_{-3.63}$	-0.799
Irr	-19.65 ± 0.36	141.19 ± 89.27	-1.31 ± 0.20	$61.86 \pm 39.11^{+16.50}_{-9.18}$	-1.417
Pec-Int	-19.43 ± 0.37	151.17 ± 48.52	-0.15 ± 0.50	$39.01 \pm 12.52^{+4.15}_{-2.15}$	-0.717
All	-19.64 ± 0.26	558.63 ± 70.24	-0.75 ± 0.20	$185.32 \pm 44.95^{+19.29}_{-10.20}$	-0.975

NOTES.—Listed are M^* , ϕ^* with its author-to-author variation, j , and the covariance between ϕ^* and L^* . The j values for the combined sample are sums over the j_{type} . All j values are given in units of the solar luminosity within the 280/40 passband, which is $M_{280} = 6.66$ in Vega units, or $2.56 \times 10^{10} \text{ W Hz}^{-1}$. A first set of errors in j is propagated from errors in ϕ^* ; the set of smaller, asymmetric errors reflect the propagation of α errors into j .

Unfortunately, the GOODS area is only one-fifth of the GEMS area, resulting in increased uncertainties from large-scale structure. We therefore address the classification bias, independent of large-scale structure uncertainties, by presenting a differential deep versus shallow comparison of GOODS- and GEMS-derived LFs for only the subsample of 290 galaxies in the GOODS area. Altogether, we present LFs for three different samples:

1. *GEMS*.—The full area with 1483 galaxies classified on shallow images, providing small statistical errors, as shown in Figure 7.

2. *GOODS-shallow*.—The central subarea of the GOODS field with 290 galaxies, classified on shallow GEMS-quality images.

3. *GOODS-deep*.—The GOODS field with 290 galaxies, classified on deep GOODS images.

The LFs of GOODS-shallow and GOODS-deep are compared in Figure 8 to assess the impact of classification bias when shallow images are used for galaxy classification.

For each LF we plot V_{max} values with error bars derived from Poisson statistics or from the author-to-author variation of the space density, whichever is greater. We overplot the best-fitting Schechter functions from a Sandage-Tammann-Yahil (STY) style fit to the sample (Sandage et al. 1979) and list their parameters in Table 1. In the left-hand panel of Figure 7 where the LF for all galaxies is shown, the lines denote the sum of the four individual type-split LFs.

Ideally, we would like to derive the Schechter function slopes independently for each data set. However, for some purposes the GEMS observations lack the sufficient depth and for some the GOODS area is not wide enough to constrain the LF shapes with high accuracy. Thus, we combined findings from both data sets to constrain the final set of Schechter functions. Hence we now discuss both Figures 7 and 8 together and list all the fine-tuning steps we have applied in STY fitting here:

E-S0 galaxies.—The GOODS-deep sample is too small to get any useful STY fit, while the GEMS sample is not deep enough. Both yield unrealistic slopes of $\alpha \sim -2$. Hence, we adopt the slope measured by Cross et al. (2004) from their deeper sample, $\alpha = 0.75 \pm 0.13$ for their combined sample of red and blue spheroids. By constraining our STY fit to this slope, we determined M^* , ϕ^* , and j_{280} from our data.

Sa-Sd galaxies.—The Schechter function for spirals is well constrained at least in GEMS and plausible in both samples ($\alpha_{\text{GEMS}} = -0.32 \pm 0.17$ and $\alpha_{\text{GOODS-deep}} = -0.52 \pm 0.41$). The LFs are determined independently.

Irregular galaxies.—In the local universe, irregular galaxies have very steep LFs with faint characteristic luminosities, making it almost impossible to estimate robust Schechter parameters if the sample is not both deep and large. Neither the GEMS nor the GOODS sample yielded particularly well-constrained faint-end slopes. We find $\alpha = -0.92 \pm 0.35$ from GEMS and $\alpha = -1.83 \pm 0.40$ from GOODS-deep. Since the V_{max} data points do not differ much and do not suggest a completely different LF, we ended up using the weighted mean of the two values, i.e., $\alpha_{\text{irr}} = -1.31 \pm 0.20$, for all Irr LFs.

Peculiar-interacting.—The slope of the Pec-Int LF in GEMS is $\alpha = +0.82 \pm 0.34$, which is biased by the incompleteness of GEMS in picking up faint mergers. For the GOODS-deep STY fit, the last data point is discarded owing to its large uncertainties, yielding a faint-end slope $\alpha = -0.15 \pm 0.50$. The increase of Pec-Int galaxies in GOODS-deep requires a corresponding decrease in other classes, because total galaxy number is conserved. The decrease is most pronounced among the irregular galaxies.

Altogether, it appears that visual classification of GEMS images biases one against faint Pec-Int galaxies. Other galaxy types are easily recognized and may be randomly confused at very low signal-to-noise ratios, but they are probably unbiased. The slopes of their Schechter functions are broadly consistent with the vast literature body of local values for blue bands.

Comparing the GOODS-shallow LF from Figure 8 with the GEMS LF in Figure 7 demonstrates the effect of cosmic variance in such small fields. In the small GOODS field we see a threefold increase in the space density of spheroids, which probably reflects the presence of several known galaxy concentrations at $z \sim 0.7$ in the central GOODS field. In contrast, we find slightly decreased abundances of spiral and Pec-Int galaxies.

4.3. UV Luminosity Density

Our data can directly address which galaxies are responsible for producing most of the UV luminosity at redshift $z \sim 0.7$, depending on their luminosity and their morphological type. We first determine how the contribution to the integrated UV light

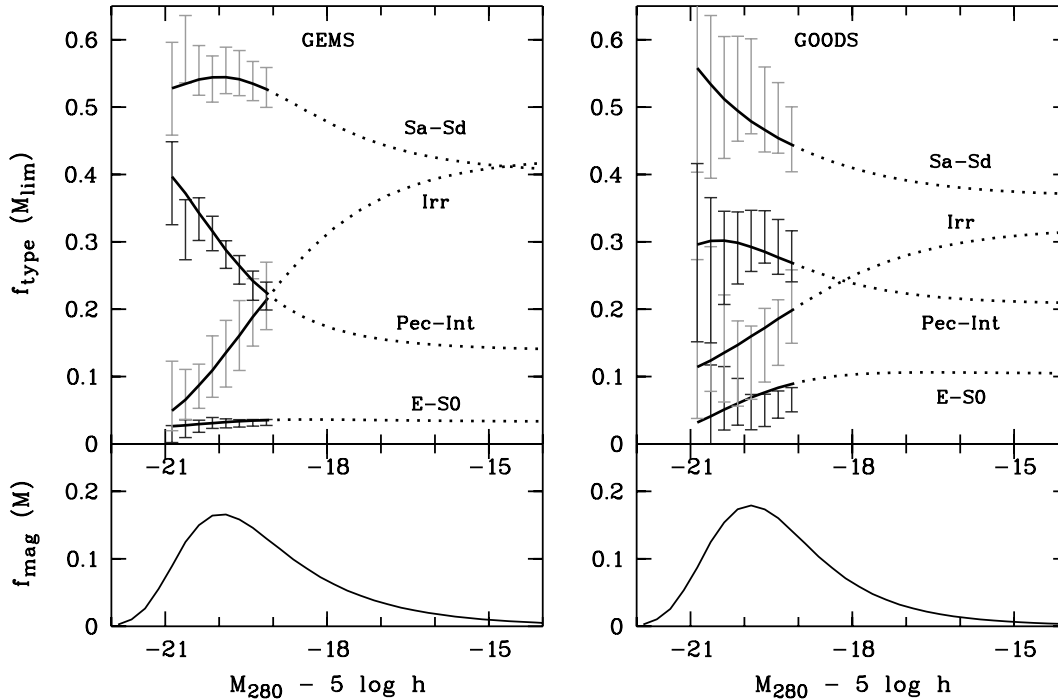


FIG. 9.—Fractional contributions to the 280 nm luminosity density from different morphological types, as derived from the wide-area GEMS mosaic (*left*) and the deeper but smaller GOODS data (*right*): *Top panels*: Contribution $f_{\text{type}}(M_{\text{lim}})$ of the four galaxy types to $j_{280}(M_{\text{lim}})$, depending on the depth to which one integrates. Thick lines are derived from the Schechter function fits. Error bars are centered on the LF data themselves and show the greater of either Poisson noise or author-to-author variation in the morphological classification. Two-thirds of the total extrapolated light is directly probed by the galaxy sample. At $M_{280} \sim -15$ the total luminosity density j_{280} and the type-dependent fractions have converged. *Bottom panels*: Contribution $f_{\text{mag}}(M)$ of magnitude intervals to the total integrated 280 nm luminosity density which peaks at $M_{280} \sim -20$, while most UV light comes from galaxies at $-21 < M_{280} < -18$.

depends on galaxy luminosity using the Schechter fits across a wide range of magnitudes. Here we define

$$f_{\text{mag}}(M) = \frac{\int_{M-0.25}^{M+0.25} L(M)\phi(M) dM}{\int_{-\infty}^{+\infty} L(M)\phi(M) dM}. \quad (2)$$

The bottom panels of Figure 9 show this fraction f_{mag} as derived from the LFs of GEMS and GOODS samples; as the total GEMS and GOODS LFs are very similar in shape, the f_{mag} distributions are almost indistinguishable. Galaxies with $M_{280} \sim -20$ make the strongest contribution to j_{280} ; the bulk of the UV light is emitted in the luminosity range $[-21, -18]$. Our observed galaxy sample itself provides 66% of the total UV luminosity density integrated from $-\infty$ to $+\infty$, which is $(4.74 \pm 1.17) \times 10^{17} \text{ W Hz}^{-1}$.

We can now estimate the fraction of UV luminosity density contributed by different galaxy types. These numbers depend on the depth to which we integrate, owing to the different Schechter parameters of the different galaxy types. The luminosity densities and their fractions by type are here defined in dependence of the limiting depth M_{lim} by

$$j_{\text{type}}(M_{\text{lim}}) = \int_{-\infty}^{M_{\text{lim}}} L(M)\phi_{\text{type}}(M) dM \quad (3)$$

and

$$f_{\text{type}}(M_{\text{lim}}) = \frac{j_{\text{type}}(M_{\text{lim}})}{\sum_{\text{type}} j_{\text{type}}(M_{\text{lim}})}. \quad (4)$$

The top panels in Figure 9 show the fractions f_{type} derived from the Schechter fits to the luminosity function as lines; solid lines

for the measured part and dotted lines where the LF is extrapolated. Because of the relatively shallow faint-end slope of the type-split LFs, f_{type} converges reasonably quickly.

Error bars show the 1σ confidence intervals of f_{type} as derived from the $\phi(M)$ measurements for the full GEMS data set (*left*) and for the deeper, smaller GOODS data (*right*). The error bars are purely statistical, reflecting either the Poissonian limitations of the sample size or the author-to-author variation in the classification, whichever is greater. They do not include contributions from cosmic variance or any systematic biases in classifications due to image depth.

With respect to these two error sources, the data from GEMS and GOODS play largely complementary roles, with each one having one advantage over the other: GEMS has a 5 times larger field, reducing the impact of cosmic variance, whereas GOODS has substantially deeper imaging data, yielding lower classification uncertainties at faint limits.

Our sample contains 66% of the total luminosity density j_{280} of the universe at $z \sim 0.7$. By integrating j_{280} only across the complete sample of galaxies in the GEMS sample at $M_{280} < -19$, we find more than $52\% \pm 3\%$ of the light originating from spirals (author-to-author variation including Poisson noise). Irregular and Pec-Int galaxies contribute $\sim 22\%$ each ($\pm 5\%$ and ± 2 , respectively), while $3.5\% \pm 0.5\%$ is from spheroids.

The GOODS sample has statistically larger error bars on all types, but less bias against faint Pec-Int galaxies. Consequently, the GOODS sample yields an increased contribution by Pec-Int galaxies to the luminosity density of $26\% \pm 4\%$. This is balanced by a decreased spiral contribution of $44\% \pm 5\%$; spheroids contribute $9\% \pm 2\%$. The fraction attributed to irregulars is largely unchanged at $21\% \pm 5\%$. Where these trends do not reflect those expected from what we expected to be primarily a

relabeling of some fraction of faint irregulars into mergers, they simply reflect the extent by which the GOODS area deviates from the cosmic average.

Figure 9 clearly shows that the relative contributions of different galaxy types is relatively insensitive to extrapolation of the UV LFs to $M_{\text{lim}} \rightarrow \infty$. Spiral galaxies are still an important source of UV light, accounting for $\sim 40\%$ of j_{280} , whereas E–S0 galaxies account for $\lesssim 5\%$. Owing to the steepness of the faint-end slope of irregular galaxies, their contribution to j_{280} may be as high as $\sim 40\%$. In contrast, owing to the decreasing importance of clear interactions toward fainter limits, even in the GOODS data, less than 25% of j_{280} is from clearly interacting galaxies, with a value of $\sim 15\%$ in the GEMS sample alone.

The propagation of errors from the LF parameters into the luminosity density is listed in Table 1, but not plotted in Figure 9. Two sources of error are explicitly addressed, which are the uncertainty in α and the error in ϕ^* at fixed M^* , which reflects just the author-to-author variation or Poisson errors, whichever is greater. The error in M^* is not propagated into j explicitly, because it is directly coupled with a compensating change in ϕ^* . The two effects cancel, if the covariance $c_{\phi^*, L^*} = -1$, which is roughly the case. The error in α is propagated by refitting the LF with α^{\pm} set to $\alpha \pm \sigma_{\alpha}$. In this procedure M^* will change due to the coupling with α , and ϕ^* will change to accommodate the new shape of the fit to the measured data points. As a result, the luminosity density will not change significantly in the measured range of luminosities, but only in the extrapolation range. The largest uncertainty comes from the ϕ^* error itself, which propagates linearly into j .

We do not actually know the shape of the LF of really faint galaxies at $z = 0.7$, but we can play with an unlikely and extreme thought experiment. Presume that *all* the faint galaxies that contribute the unobserved one-third of the total UV light belong to a single morphological class, whereas the other three respective classes exist only at the observed bright magnitudes. While this scenario is completely unrealistic, it would increase the j_{280} fraction of the then dominant type above the previously stated numbers by the highest possible degree. Rotating through the four classes as sole constituents of faint galaxies, we find their absolute-maximum values, $f_{\text{type, max}} \approx 35\%$, 65%, 50%, and 50% for E–S0, Sa–Sd, Irr, and Pec-Int, respectively.

5. DISCUSSION

We motivated our analysis with the observation that at the present day the 280 nm luminosity density is a factor of 3–6 lower than at $z = 0.7$. This drop must reflect a strong decrease in the UV luminosity of the largest contributors at $z = 0.7$, i.e., the spirals and the faint blue irregulars. A drop in the UV luminosity of ongoing mergers is expected also; however, they account for less than a quarter of the UV light at $z \sim 0.7$ to start with. Therefore, the evolution of such mergers (even if they had completely disappeared by $z = 0$) cannot be the primary driver of the overall change in the UV luminosity density and the unobscured SFR of the galaxy population.

5.1. Comparison of Galaxy Colors

The fraction of spheroids with blue colors has been measured by various authors at around 30%–40% and is possibly not a strong function of redshift between $z \sim 0.3$ and $z \sim 1$ (Cross et al. 2004; Menanteau et al. 2004; Stanford et al. 2004). We measure fractions between 30% and 40% as well, depending mostly on the choice of rest-frame band (*UBV*) and magnitude limits but also on the precise choice of the red-sequence cut. Stanford et al. (2004) found more than 50% blue members in a

spheroid sample selected in the near-IR on NICMOS images. However, many of their blue spheroids appear like late-type galaxies in optical bands from WFPC2. Menanteau et al. (2004) investigated spatially resolved color maps of spheroids at $z \lesssim 1$ from *HST* images and found predominantly blue cores, but also inhomogeneous internal colors suggestive of an early stage in the formation of spheroids.

We found the merger candidates to have a color distribution similar to that of spirals with only a slight shift to the blue, while the irregular galaxies are distinctively bluer than both the average merger and average spiral. The same result has been reported by Conselice et al. (2003). This distribution has also been found in the local universe by Bergvall et al. (2003), who found the colors of interacting galaxies to be only slightly bluer than those of noninteracting galaxies at $z \sim 0$. They observed also similar L_{FIR}/L_B ratios in both samples, leaving no room for strong obscured starbursts.

5.2. Comparison of Luminosity Densities

The *HST* observations in the Canada-France Redshift Survey (CFRS) fields were seminal in this field, but limited by sample size and depth. In their first paper, Brinchmann et al. (1998, hereafter CFRS1) examined the types of galaxies contributing to the *B*-band luminosity from $z \sim 0.9$ to $z \sim 0.3$. CFRS1 used three galaxy types, i.e., spirals, ellipticals, and irregulars, including ongoing violent mergers, and found most of the decline in j_B to be a result of the evolution of spiral galaxies, which dominate j_B at the high- z end. Brinchmann et al. found that the *B*-band contribution from irregulars dropped at least as much as that of the spirals, although they provided a smaller contribution to begin with.

While this is fully consistent with our observations, the *B*-band luminosity reflects a broad range of stellar ages and the decline in luminosity density is less pronounced than in the UV. Dickinson et al. (2003) found that j_B declines by a factor of 2.5 from $z \sim 1$ to $z \sim 0$, and Wolf et al. (2003) found a factor of ~ 2 , which are flatter than the decline in the UV. Our results, determined in the UV, show that irregulars plus visible mergers contribute more to j_{280} than the spirals once we include the faint regime. This is a natural result of irregulars being bluer on average than spirals and appearing relatively more luminous in the UV.

In terms of stellar mass, Brinchmann & Ellis (2000) found spheroid, disk, and irregular galaxies to account for roughly one-third of the stellar mass each at $z \sim 1$. Toward the present day the mass fraction in irregulars drops to $\sim 2\%$ of the total. The disappearing stellar mass from irregulars appears as a mass increase among the regular morphological types, which is either a result of merging or a consequence of more regular star formation patterns being established in an initially irregular galaxy.

In a recent paper, Conselice et al. (2005) finally show that 90% of the blue luminosity density at $z \sim 1$ originates from spirals and spheroids in roughly equal parts, leaving only 10% to irregulars and merging galaxies. They conclude that at $z < 1$ galaxies grow mostly through minor mergers or quiescent star formation driven by gas infall, while major mergers are only dominating at $z > 2$.

5.3. Comparison of Merger Fractions

The fraction and rate of galaxy mergers was estimated by various authors at different redshifts and luminosities. Le Fèvre et al. (2000, hereafter CFRS4) used visual classification of the CFRS galaxy sample observed with *HST*. They found a dramatic increase in galaxies with merger morphologies toward

higher redshift, reaching a fraction of 10% at $z \sim 0.63$ and even $\sim 20\%$ at $z \sim 0.9$ (selected with $I_{AB} < 22.5$). Their results reflect the merger rate at the high-luminosity end, where we have also found interacting galaxies to be quite abundant. If we limit our sample to $I_{AB} = 22.5$, then we find a merger fraction of 14% at $z \sim 0.7$, consistent with those of CFRS4. We note that at $z \sim 0.7$ the observed-frame I -band selection corresponds to a rest-frame B -band selection, which is also used by several other studies.

CFRS4 conjectured that mergers could be even more abundant among galaxies of lower luminosity. Our analysis implies that this is not the case. Although recognizable mergers are very common at the highest of all UV galaxy luminosities, their LF rises less quickly than the LF of the total galaxy population. Therefore, the integrated fraction of classifiable mergers actually drops with fainter UV luminosity.

While incompleteness of mergers among faint galaxies is a concern, contamination due to projection effects or large star-forming regions may also be a problem. In fact, Bundy et al. (2004) suggest that major merger and close pair fractions determined in the optical at $z \sim 1$ may be inflated by bright star-forming regions that are unlikely to be representative of the underlying mass distribution. Using K -band observations, they derive the fraction of pairs that will produce major mergers within ~ 1 Gyr. These fractions are much lower than optical bands would suggest for the same galaxy sample, because many companions in the optical are particularly blue. Hence, they have lower masses than suggested by their light contribution, and lead only to minor mergers. As a result of selecting in the K band, they find less than 10% mergers at $z \sim 1$, where *HST*-band data suggested $\sim 20\%$.

Conselice et al. (2003) measured the merger rate using automated measures of morphological disturbance in the rest-frame B band from $z \sim 3$ to the present day using the Hubble Deep Field–North (Williams et al. 1996). Their results show an increasing merger fraction with increasing luminosity; at $z \sim 0.6$ they find a 4% merger fraction at $M_B < -18$ and 7% mergers at $M_B < -20$. Their overall fraction is lower than the one derived in this paper, but bearing in mind the small field size and differences in methodology, the agreement is not unreasonable.

Studies of close pairs of galaxies can also constrain merger rate. To date, they have typically inferred rather lower merger rates than morphological studies. Patton et al. (2002) found that 15% of galaxies with $-21 < M_B < -18$ have undergone a major merger since $z \sim 1$ using dynamically close pairs from the CNOC2 survey. Recently, Lin et al. (2004) used a sample of wide-separation pairs to estimate the merger rate, finding that rather fewer than 10% of present-day L^* galaxies have undergone a major merger since $z \sim 1$, although with considerable uncertainties owing to the use of wide-separation pairs. They suggested that studies using morphological criteria to identify mergers may pick up many minor mergers as well, which should help to explain the disagreement.

Irrespective of whether major mergers are defined morphologically or via close pairs, it appears that recent work converges to the conclusion that most stellar mass formed at $z < 1$ is not formed via starbursts in major mergers, while the opposite may well be true at $z > 2$ (Conselice et al. 2003, 2005).

5.4. Effects of Dust Extinction

The impact of extinction by dust is a significant uncertainty affecting the interpretation of rest-frame UV luminosities. This is of particular concern in this study, as dust extinction is known to

depend on gas content, metallicity, geometry, and stellar age—all factors that correlate strongly with morphological type. Therefore, we cannot immediately conclude that contributions of various galaxy types to the UV luminosity density reflect their relative contributions to the cosmic-average SFR.

Yet, an understanding of the contribution of different galaxy types to the UV luminosity density is important, both because it is possible to reach down well below the knee of the luminosity function and because an understanding of the UV luminosity density gives some insight into, e.g., plausible sources of ionizing UV photons. Bell et al. (2005) use deep $24 \mu\text{m}$ data from *Spitzer* to explore the importance of obscured star formation for the same $0.65 < z < 0.75$ sample of galaxies used in this paper. Roughly one-third of the GEMS sample are detected at $24 \mu\text{m}$, accounting for more than half (likely \sim two-thirds) of the total SFR at $z \sim 0.7$. They find many highly obscured galaxies, with $\text{IR}/\text{UV} \gtrsim 10$. Yet, despite this dominant contribution from the IR, the qualitative picture is very similar: $\lesssim 40\%$, and more likely $\sim 30\%$, of the total SFR (as derived from the IR and UV luminosities combined) is in clearly interacting systems, with the rest coming primarily from spiral galaxies with small contributions from irregulars and E–S0 galaxies. Their results are fully consistent with earlier *Infrared Space Observatory* results (e.g., Flores et al. 1999; Zheng et al. 2004), with the important advantages of increased sample size and sensitivity. This supports the primary conclusion of this paper: a decreasing major merger rate cannot be the dominant driver of the drop in cosmic SFR between $z \sim 1$ and the present day.

5.5. Expectations from Hierarchical Models

The hierarchical structure formation paradigm within a given cold dark matter cosmology makes specific predictions for the evolution of the merger rate of dark matter halos as a function of time. However, converting this to quantities that can be directly compared with the observations presented here involves several uncertain steps. First, the amount of star formation associated with mergers depends on the details of the star formation and feedback recipes implemented in the models. Second, we need to distinguish between two questions, one of which is physically more interesting and the other of which is what is observationally addressed in this paper:

1. What fraction of the total star formation at a given epoch is caused by a merger-triggered burst?
2. What fraction of the total star formation is contributed by galaxies that appear morphologically disturbed?

Based on hydrodynamic simulations, it is likely that the timescale over which galaxies appear morphologically disturbed following a merger is considerably longer (about a factor of a few to 10) than the timescale over which star formation is significantly enhanced (e.g., Cox et al. 2005). As well, galaxies with low gas fractions may not experience a significant star formation episode in a merger event.

In order to address this question in a way that can be directly related to the observational results presented here, we made use of a GEMS mock catalog created using a semianalytic model similar those presented in Somerville et al. (2001, hereafter SPF). The global SFR density produced by this model is in good agreement with dust-corrected observational estimates from $z \sim 0$ to 6 (SPF; Giavalisco et al. 2004), and the model also reproduces many (although not all) observational properties of low- and high-redshift galaxies. We assume that a galaxy would be identified as “morphologically disturbed” if it has experienced

a major merger (1:4 or greater mass ratio) within a timescale $\tau_{\text{dist}} = \eta t_{\text{dyn}}$, where t_{dyn} is the internal dynamical time of the galaxy and η is a factor of order a few. Here we use $\eta = 2$. We consider galaxies in a redshift slice $0.65 < z < 0.75$, as for the GEMS sample. For a model similar to the “collisional starburst” model described in SPF, in which both major and minor mergers trigger bursts of star formation, we find that 30% of the star formation is contributed by these “strongly disturbed” galaxies. We find that 53% of the star formation is contributed by galaxies that have experienced a merger down to a mass ratio of 1:20 within the timescale τ_{dist} systems.¹¹ Varying the recipes for quiescent and burst star formation to encompass alternative choices commonly made in the literature (see, e.g., SPF), we obtain a range of values between 12% and 33% for the fraction of star formation in strongly disturbed galaxies (major mergers). This result does not change significantly for values of η in the range 1–10, and the fractions are similar for a magnitude-limited sample selected with the GEMS/COMBO limit $R < 24$. We present a more detailed description of the models and the dependence on the model ingredients in a subsequent paper (R. S. Somerville et al. 2005, in preparation).

We can compare these results with the predictions that may be read directly from Figures 10 and 11 of SPF, which show the SFR contributed by quiescent and actively bursting galaxies. Based on those figures, the collisional starburst model predicts that 35% of star formation at $z = 0$ is due to bursts in galaxy interactions of all mass ratios, while only 2.5% arises from major (4:1 or greater) mergers. At $z = 0.7$, about 50% of the star formation is from bursts of all types, with only 5% arising from bursts associated with major mergers. At $z = 3$, the model predicts that 75% of all star formation is due to collisional starbursts, while 18% is due to major-merger-induced bursts. It is important to keep in mind, however, that the timescale of the starburst assumed in this tabulation was assumed to be $\sim 0.1 t_{\text{dyn}} - 1 t_{\text{dyn}}$. This factor of $\sim 2 - 10$ difference between the duration of the burst and the duration of the morphologically disturbed phase, assumed above, accounts for most of the difference between the values of 5% from SPF and the values quoted above.

For comparison, in the semianalytic model of Cole et al. (2000), only 5% of the star formation at $z \sim 0.7$ is contributed by the burst mode (bursts were assumed to occur only in major mergers in this model). In the updated model of Baugh et al. (2005), 16% of the star formation at $z \sim 0.7$ is from bursts of *all types* (major+minor). The new Baugh et al. model includes bursts in minor mergers, but only when the gas fraction is above a critical value. Again, these results only record the star formation during the relatively short burst phase, and they do not take into account the longer timescale of the morphologically disturbed phase.

6. SUMMARY

We have investigated the contribution of galaxies of different morphological type to the UV luminosity density of the universe at $z \sim 0.7$. The goal was to understand in which kind of galaxies the observed decline in the UV luminosity density occurred between this epoch and the present day. The experiment has shed light on the physical processes behind this drop in cosmic SFR. In particular, we have placed constraints on the

fraction of the UV luminosity density arising from clearly interacting galaxies at $z \sim 0.7$.

Our analysis was based on a sample of 1483 galaxies in a thin redshift slice at $0.65 < z < 0.75$ in the COMBO-17/GEMS field encompassing the CDF-S. We have used rest-frame luminosities at 280 nm and in the V band from COMBO-17 together with three independent visual morphological classifications from rest-frame V -band images from the GOODS and GEMS *HST* ACS surveys. We differentiated between four broad morphological types: spheroid-dominated (E–S0), disk-dominated (Sa–Sd), irregular (Irr), and peculiar or clearly interacting galaxies with morphological features indicative of ongoing major mergers (Pec-Int). The difference between Irr and Pec-Int is driven primarily by a desire to identify the cause of irregular morphological appearance; galaxies with morphologies consistent with the stochastic propagation of star formation were labeled irregular, while galaxies with features indicative of strong gravitational disturbance, such as multiple nuclei or tidal tails, were labeled Pec-Int.

Comparing the morphological classifications between the shallower GEMS images and the deeper GOODS images, we have established that GEMS images do not allow for a complete identification of merging galaxies in the faintest magnitude bin we consider. This causes an artificially steep downturn in the luminosity function of mergers from the GEMS sample. Compensating for this shortcoming, the GEMS data offer the important advantage of a much larger galaxy sample, with properties closer to the cosmic average, than GOODS.

We analyzed UV–optical CMDs, UV luminosity functions, and luminosity densities j_{280} for all morphological types of galaxies. We found that although interacting and violently merging galaxies dominate the rare group of particularly blue and very luminous objects, their rest-frame colors are similar to those of otherwise normal spirals.

We found that seemingly normal disk galaxies (Sa–Sd) are the largest contributor to the UV luminosity density, emitting about half of the j_{280} at $z \sim 0.7$ and $M_{280} < -19$. The observed galaxy sample contributes 66% of the total extrapolated j_{280} from the entire galaxy population. After extrapolation, spiral galaxies emit $\sim 40\%$ of the total UV luminosity density. The second largest contribution originates from irregulars, which are predominantly faint and blue. Their steep luminosity function drives their contribution up to about 40% of the total j_{280} . Most of the remaining UV light comes from interacting systems and ongoing violent mergers, while the contribution from spheroids is negligible. The exact number for the merger contribution depends to some extent on the completeness of identification and the precise shape of their faint LF, but it is likely to be around 20%. We find that these results are consistent with predictions from a semianalytic galaxy formation model similar to the collisional starburst model of Somerville et al. (2001).

The results presented here demonstrate clearly that the drop in the UV luminosity density of the universe since $z = 1$ largely reflects decreasing SFRs in normal spirals. In parallel, high SFRs in faint blue irregulars are migrating to systems of progressively lower mass and luminosity. Any evolution in the major merger rate plays only a small role in the decline of unobscured star formation. It would be relevant for driving the decline of star formation since $z = 1$ only if the drop in the cosmic SFR were substantially steeper than that inferred in the UV and if the average extinction levels in mergers were far above the average of highly star-forming, but otherwise normal, spiral galaxies. First analyses of 24 μm data from *Spitzer* (Bell et al. 2005; Le Floc’h et al. 2005) have started to address these issues,

¹¹ It is worth noting, however, that even in a model in which we assume that minor mergers do not trigger bursts, we find that 51% of the star formation is “associated” with minor mergers. This illustrates the ever-present danger of equating correlation with causality.

and support the conclusion of this paper that merging systems do not dominate the $z \lesssim 1$ SFR.

Support for the GEMS project was provided by NASA through grant GO-9500 from the Space Telescope Science Institute, which is operated by the Association of Universities for Research in Astronomy, Inc., for NASA, under contract NAS5-26555. E. F. B. and S. F. S. acknowledge financial support provided through the European Community's Human Potential Program under contract HPRN-CT-2002-00316, SISCO (E. F. B.), HPRN-CT-2002-00305, and Euro3D RTN (S. F. S.). S. J. acknowledges

support from the NASA under LTSA grant NAG5-13063 issued through the Office of Space Science. D. H. M. acknowledges support from NASA under LTSA grant NAG5-13102 issued through the Office of Space Science. C. Y. P. acknowledges support from NASA/JPL, under the Michelson Fellowship Program. JPL is managed for NASA by the California Institute of Technology. C. H. acknowledges support from the German-Israeli-Foundation (GIF). K. J. was supported by the German DLR under project number 50 OR 0404. C. W. is supported by a PPARC Advanced Fellowship. We thank an anonymous referee for numerous helpful comments and Sadegh Khochfar for improving the manuscript.

REFERENCES

- Baldry, I. K., et al. 2004, *ApJ*, 600, 681
 Baugh, C. M., Cole, S., Frenk, C. S., & Lacey, C. S. 1998, *ApJ*, 498, 504
 Baugh, C. M., et al. 2005, *MNRAS*, 356, 1191
 Bell, E. F., & de Jong, R. S. 2001, *ApJ*, 550, 212
 Bell, E. F., et al. 2004, *ApJ*, 608, 752
 ———. 2005, *ApJ*, 625, 23
 Bergvall, N., Laurikainen, E., & Aalto, S. 2003, *A&A*, 405, 31
 Bouwens, R. J., et al. 2003, *ApJ*, 595, 589
 Brinchmann, J., & Ellis, R. S. 2000, *ApJ*, 636, L77
 Brinchmann, J., et al. 1998, *ApJ*, 499, 112 (CFRS1)
 Bundy, K., Fukugita, M., Ellis, R. S., Kodama, T., & Conselice, C. J. 2004, *ApJ*, 601, L123
 Bunker, A. J., Stanway, E. R., Ellis, R. S., & McMahon, R. G. 2004, *MNRAS*, 355, 374
 Carlberg, R., et al. 2000, *ApJ*, 532, L1
 Cen, R., & Ostriker, J. P. 1999, *ApJ*, 514, 1
 Cole, S., Lacey, C. G., Baugh, C. M., & Frenk, C. S. 2000, *MNRAS*, 319, 168
 Conselice, C. J. 2003, *ApJS*, 147, 1
 Conselice, C. J., Bershad, M. A., Dickinson, M., & Papovich, C. 2003, *AJ*, 126, 1183
 Conselice, C. J., Blackburne, J. A., & Papovich, C. 2005, *ApJ*, 620, 564
 Cowie, L. L., Songaila, A., & Hu, E. M. 1996, *AJ*, 112, 839
 Cox, T. J., Jonsson, P., Primack, J. R., & Somerville, R. S. 2005, *MNRAS*, submitted (astro-ph/0503201)
 Cross, N. J. G., et al. 2004, *AJ*, 128, 1990
 Dickinson, M., Papovich, C., Ferguson, H. C., & Budavari, T. 2003, *ApJ*, 587, 25
 Flores, H., et al. 1999, *ApJ*, 517, 148
 Giavalisco, M. 2002, *ARA&A*, 40, 579
 Giavalisco, M., et al. 2004, *ApJ*, 600, L93
 Gilli, R., et al. 2003, *ApJ*, 592, 721
 Haarsma, D. B., Partridge, R. B., Windhorst, R. A., & Richards, E. A. 2000, *ApJ*, 544, 641
 Hernquist, L., & Springel, V. 2003, *MNRAS*, 341, 1253
 Kennicutt, R. 1998, *ApJ*, 498, 181
 Le Fèvre, O., et al. 2000, *MNRAS*, 311, 565 (CFRS4)
 ———. 2004, *A&A*, 428, 1043
 Le Floch, E., et al. 2005, *ApJ*, in press
 Lilly, S. J., Le Fèvre, O., Hammer, F., & Crampton, D. 1996, *ApJ*, 460, L1
 Lin, L., et al. 2004, *ApJ*, 617, L9
 Lotz, J. M., Primack, J., & Madau, P. 2004, *AJ*, 128, 163
 Madau, P., Pozzetti, L., & Dickinson, M. 1998, *ApJ*, 498, 106
 Madau, P., et al. 1996, *MNRAS*, 283, 1388
 Menanteau, F., Abraham, R. G., Madau, P., Pozzetti, L., & Dickinson, M. 1998, *MNRAS*, 322, 1
 Menanteau, F., et al. 2004, *ApJ*, 612, 202
 Nagamine, K., Cen, R., & Ostriker, J. 2000, *ApJ*, 541, 25
 Patton, D. R., et al. 2002, *ApJ*, 565, 208
 Pei, Y. C., Fall, S. M., & Hauser, M. G. 1999, *ApJ*, 522, 604
 Rieke, G., et al. 2004, *ApJS*, 154, 25
 Rix, H.-W., et al. 2004, *ApJS*, 152, 163
 Sandage, A., Tammann, G. A., & Yahil, A. 1979, *ApJ*, 232, 352
 Sanders, D. B., & Mirabel, I. F. 1996, *ARA&A*, 34, 749
 Somerville, R. S., Primack, J. R., & Faber, S. M. 2001, *MNRAS*, 320, 504
 Springel, V., & Hernquist, L. 2003, *MNRAS*, 339, 312
 Stanford, S. A., et al. 2004, *AJ*, 127, 131
 Storrie-Lombardi, L. J., McMahon, R. G., & Irwin, M. J. 1996, *MNRAS*, 283, L79
 Strateva, I., et al. 2001, *AJ*, 122, 1861
 Sullivan, M., et al. 2000, *MNRAS*, 312, 442
 Wang, B., & Heckman, T. M. 1996, *ApJ*, 457, 645
 Williams, R. E., et al. 1996, *AJ*, 112, 1335
 Wilson, G., Cowie, L. L., Barger, A. J., & Burke, D. J. 2002, *AJ*, 124, 1258
 Wolf, C., Meisenheimer, K., & Röser, H.-J. 2001, *A&A*, 365, 660
 Wolf, C., et al. 2003, *A&A*, 401, 73
 ———. 2004, *A&A*, 421, 913
 Yan, L., et al. 1999, *ApJ*, 519, L47
 Zheng, X. Z., Hammer, F., Flores, H., Assémat, F., & Pelat, D. 2004, *A&A*, 421, 847